Vol 15 No 4, April 2006
1009-1963/2006/15(04)/0659-06

Chinese Physics

© 2006 Chin. Phys. Soc.
and IOP Publishing Ltd

Elaborate calibration procedure for cell irradiation at the CAS-LIBB single-particle microbeam*

Hu Zhi-Wen(胡智文)[a)b)], Ding Ke-Jian(丁克俭)[a)], Yu Liang-Deng(余量登)[c)], Zhang Jun(张 俊)[a)], Wu Li-Jun(吴李君)[a)], and Yu Zeng-Liang(余增亮)[a)†]

[a)] *Key Laboratory of Ion Beam Bioengineering, Institute of Plasma Physics, Chinese Academy of Sciences, Hefei* 230031, *China*
[b)] *Department of Computer Science and Technology, Huaibei Coal Industry Teachers College, Huaibei* 235000, *China*
[c)] *Department of Physics, Faculty of Science, Chiang Mai University, Chiang Mai* 50200, *Thailand*

(Received 8 September 2005; revised manuscript received 17 January 2006)

Single-particle microbeam is uniquely capable of precisely delivering a preset number of charged particles to individual cells or sub-cellular targets to be determined *in vitro*. It is crucial to find a reference point that relates the microbeam's location to the microscope's plane, and align individual targets at this reference point for cell irradiation. To choose an appropriate reference point, an approach based on analysing the intensity distribution of fluorescence in a thin scintillator excited by traversing particles is newly developed using the CAS-LIBB single-particle microbeam, which features decisive physical signification and sufficient resolution. As its bonus, this on-line analysis provides precise and fast response to the determination of beam profile and potentially optimizes the microbeam quality by further adjusting hardware setup.

Keywords: single-particle microbeam, calibration procedure, cell irradiation, targeting accuracy
PACC: 0150P, 2921, 0777, 8780

1. Introduction

All biological effects of ionizing radiation are derived from events that take place at the level of individual cells. The radiation of charged particle beams deposits their energies in target regions surrounding the travelling paths of the particles. The random interactions of the particles as well as secondary particles such as displaced atoms with different parts of a cell can cause some effects. In the process, inter- and intra-cellular signaling pathways play an important role. However, the biological effects of radiation spread beyond the field that is directly subject to hits from the ionizing radiation tracks — known as the physical penumbra. The limits of spread — known as the biological penumbra — are unknown and might be systemic.[1] Therefore, we have developed a novel microbeam technique to study effects of radiation tracks on induced damage and initiation processes in critical cellular targets.

The single-particle microbeam (SPM) provides a unique opportunity to precisely control the number of ions traversing individual cells and the localization of dose within the cells *in vitro*. There exist currently more than 15 SPMs in the world and they are still improved. Their recent developments and applications are reviewed.[2−7] A single-particle microbeam facility using the collimation technique, CAS-LIBB SPM, has been built at the Key Laboratory of Ion Beam Bioengineering (LIBB), Chinese Academy of Sciences (CAS), Hefei, China.[8−12]

For a collimated SPM, it is crucial to find a reference point of beam exit and align individual targets at this reference point for highly-localized cell irradiation. Folkard *et al* suggested a calibration procedure wherein the reference position was established by simply imaging the top of the collimator for visual interpretation.[13] Randers-Pehrson *et al* reported that the reference point of beam exit was defined by grabbing images of laser light directing to the colli-

*Project supported by the National Major Technology Research and Development Program of China during the 10th Five-Year Plan Period (Grant No 2001BA302B), the National Science Fund for Distinguished Young Scholars of China (Grant No 10225526), the Knowledge Innovation Program of the Chinese Academy of Sciences (Grant No KSCX2-SW-324), and the Foundation for University Key Teacher by the Ministry of Education, China (Grant No 2005jq135).

†E-mail: zlyu@ipp.ac.cn

mator system from below the last bending magnet.[14] In fact, the physical signification of reference point is that the probability of traversing particles appearing there is maximum. To choose an appropriate reference point, an approach based on analysing the intensity distribution of fluorescence in a thin scintillator excited by traversing charged-particles is newly developed using the CAS-LIBB single-particle microbeam, which features decisive physical signification and sufficient resolution. Furthermore, this on-line analysis possesses the capability to determine beam profile accurately and can optimize the microbeam quality by further adjusting hardware setup.

2. Materials and methods

2.1. CAS-LIBB microbeam facility

The source of ions for the CAS-LIBB microbeam is generated by a model CN 5.5 MV van de Graaff accelerator. Most of work to date on the microbeam has been done with protons of 3 MeV corresponding to a linear energy transfer (LET) of approximately 30 keV/μm at the centre of the cells. After passing through quadrupole magnets and two beam bending magnets, the monoenergetic beam goes vertically through collimator. Figure 1 shows the overall layout of the microbeam endstation and the collimator. The custom-made dish is supported on a motorized X-Y microscope stage (Märzhäuser Wetzlar GmbH, Germany) that is positioned using a stepper-motor coupled lead-screw on each axis. The cells can be viewed *in situ* using an epi-fluorescent microscope (Olympus, type BX2-FLB), either through the eyepiece, or more often, with an image intensifier (Dage-MTI Inc., Michigan City, IN) and a charge-coupled device (CCD) (CCD-72E, Dage-MTI Inc., Michigan City, IN) imaging system. The CCD image is digitized (12 bits) and transferred to a Matrox 1280 image processing board (Matrox Electronic Systems, Dorval, Canada) installed in a personal computer, and it is displayed on a high-resolution monitor. A borosilicate glass capillary with 1 μm in inner diameter, 210 μm in outer diameter and 980 μm in length is used as a collimator, which is mounted in the centre of a holder at the end of the beam line. The verticality of the collimator is adjustable with fine adjustment screws. A multilayer film system composed of a 3.5-μm vacuuming Mylar film, a 7-μm aluminium photon-reflector and an 18-μm scintillator film (Bicron, BC400) for particle detection, which are piled in layers, is mounted on the collimator exit. The exit of the assembly is covered with another piece of 3.5-μm mounting Mylar, as shown in Fig.1.

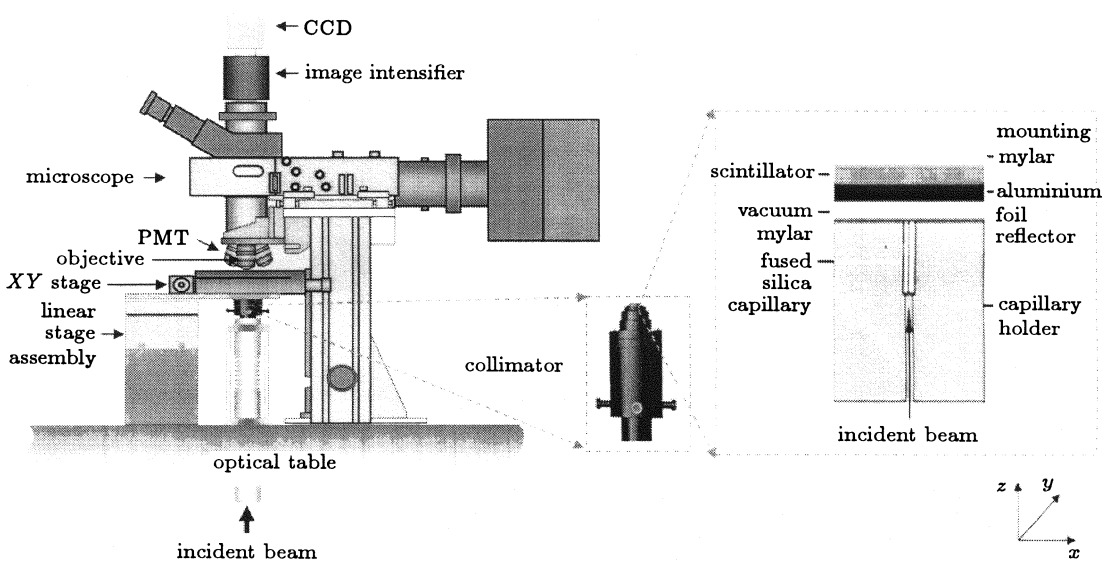


Fig.1. Schematic drawing of the overall layout of the microbeam endstation and the installation of the collimator.

2.2. Basic principle of beam profile determination

Monte Carlo modelling of the proton transmission in a borosilicate glass capillary with an aspect ratio of 980:1, compared with the energy spectrum of the transmitted particles, indicates that about >99%

of the protons are within the nonscattering core of the beam, which initially has a diameter of 1 μm and spreads little more than 1 μm due to Coulomb scattering in the exit window. Since the de Broglie wavelength of an accelerated proton in the CAS-LIBB microbeam is about 10^{-4}Å, much smaller than the dimension of the medium, the wave-effect of these particles can be neglected when they are transferred, that is, the particles-transferring process can be regarded as line-transfer. It is reasonable to assume that the scintillator is homogeneous and individual traversing particles produce equal photon yields. On this assumption, the bombarding beam profile that one can observe at the target only depends on the interaction between the beam particles and the target. The interaction surface between the scintillator and traversing particles can be regarded as a plane. The total number of reaction products, N, can be formulated by

$$N \propto \iint_{S_s} D\,(x,y)\,n\,(x,y)\,\mathrm{d}x\mathrm{d}y, \tag{1}$$

where S_s is the total interaction area, $n(x,\ y)$ is the beam particle distribution in the beam cross section, $D(x,\ y)$ is the scintillator's mass distribution that is usually considered as a constant, D, and x and y are the coordinates in the interaction or scintillator plane. If the beam scans a unit square in $(x,\ y)$ directions, and then scans the whole plane, square by square, on the scintillator plane, Eq.(1) can be used to express the total number of the reaction products for the $(i,\ j)$th square as

$$N_{i,j} \propto D \iint_{\text{square}} n(x,y)\mathrm{d}x\mathrm{d}y. \tag{2}$$

The integral actually represents the total number of the particles, or the particle flux, falling into the square. The count difference, $N_{i+1,j+1}$–$N_{i,j}$, between two sequential scanning positions is proportional to the flux, which passes through a micro-square with the sides of $\Delta x = x_{i+1} - x_i$ and $\Delta y = y_{i+1} - y_i$.

The plastic scintillator (PS), BC400 ($C_{10}H_{11}$), consists of a polyaromatic hydrocarbon base, polyvinyltoluene (PVT), containing one or two fluorescent dyes. Energy absorbed from ionizing radiation excites the base molecules, which non-radiatively transfer the energy to primary dye molecules. The dye molecules in turn emit primary scintillation photons that are wave-shifted to longer wavelengths by the secondary dye. Ideally, a PS dosimeter should have a scintillation efficiency independent of the energy and type of ionizing radiation particle, and the light output would be proportional to the energy deposited in the scintillator. However, it is well known that the PS sensitivity is reduced for high-LET radiations such as alpha particles, low-energy protons and deuterons(Figure 2).[15,16] It is thought that dense ionizing charged particle tracks give rise to reactive molecular species which can dissipate the excitation energy of solvent or solute particles, competing with radiative de-excitation (fluorescence).[17] The progressive loss of light output with the LET or stopping power increasing is usually explained by ionization quenching: creation of excited/ionized molecular species by dense ionizing charged particles that inhibit light emission nearby collision sites. The reported data generally support the well-known unimolecular-quenching model proposed by Birks:

$$\mathrm{d}L/\mathrm{d}x = \frac{S(\mathrm{d}E/\mathrm{d}x)}{1 + k_{\mathrm{B}}(\mathrm{d}E/\mathrm{d}x)}, \tag{3}$$

where $\mathrm{d}L/\mathrm{d}x$ is the differential light output, $\mathrm{d}x$ is the path length traversed by the charged particles, S is the absolute (unquenched) sensitivity, $\mathrm{d}E/\mathrm{d}x$ is the collisional stopping power and k_{B} is Birks' parameter, which is reported to range from 0.0066 to 0.019 cm MeV^{-1} for unit-density scintillators.[18]

By integrating Eq.(3) over the electron slowing-down spectrum, the inherent sensitivity, $\alpha(E)$, of a PS to the complete absorption of a secondary electron with an initial energy of E can be derived as follows:

$$\alpha(E) = \frac{S}{E}\int_0^E [1 + k_{\mathrm{B}}(\mathrm{d}E/\mathrm{d}x)]^{-1}\mathrm{d}E. \tag{4}$$

By averaging $\alpha(E)$ over the spectrum of initial kinetic energies of the secondary electrons movement caused by photon collisions, α_λ can be evaluated:

$$\begin{aligned}\alpha_\lambda =& \left\{ S\int_0^{v_{\max}} \Phi_\lambda(v)\left[\sigma_{\mathrm{pe}}(v)(v - E_{\mathrm{K}})\alpha(v - E_{\mathrm{K}}) \right.\right. \\ &\left.\left. + \int_0^\pi \frac{\mathrm{d}\sigma_{\mathrm{inc}}(v,\theta)}{\mathrm{d}\Omega}E(v,\theta)a(E(v,\theta))\sin\theta\mathrm{d}\theta\right]\mathrm{d}v\right\} \\ &\times \left\{ \int_0^{v_{\max}} \Phi_\lambda(v)\left[\sigma_{\mathrm{pe}}(v)(v - E_{\mathrm{K}}) \right.\right. \\ &\left.\left. + \int_0^\pi \frac{\mathrm{d}\sigma_{\mathrm{inc}}(v,\theta)}{\mathrm{d}\Omega}E(v,\theta)\sin\theta\mathrm{d}\theta\right]\mathrm{d}v\right\}^{-1}, \end{aligned} \tag{5}$$

where v is photon energy, $\Phi_\lambda(v)$ is the photon fluence in the detector centre, E_{K} is the K-edge binding energy, σ_{pe} is the photoionization cross section, $\mathrm{d}\sigma_{\mathrm{inc}}/\mathrm{d}\Omega$ is the differential cross section for incoherent scattering and $E(v,\theta)$ is the initial kinetic energy

of Compton electrons scattered at an angle θ. Therefore, the fluorescent intensity distribution may directly reflect the responsive beam particle distribution.

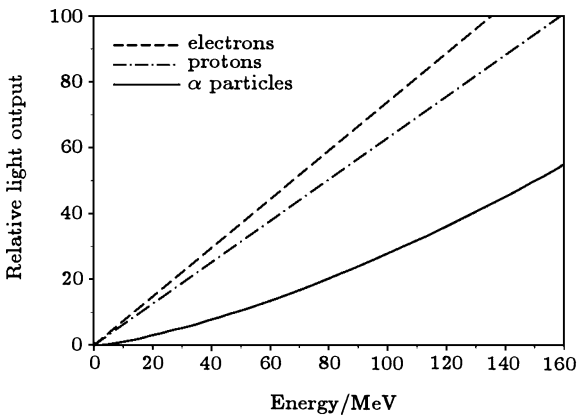


Fig.2. Premium BC400 response to atomic particles.

2.3. Choosing a reference point and aligning targets at beam exit for irradiation

For cell image processing, at first the position of the microbeam exit is located by a program as the reference point. The cell image recognition and processing are carried out jointly using the microscope, the image intensifier, the CCD camera and the image processing board using the Matrox Imaging Library (Matrox Electronic Systems, Dorval, Canada) in a computer. A series of fluorescent images of weak spots excited by traversing particles bombarding the scintillator is recorded by this imaging subsystem. We can obtain a series of sharp images from these beam profiles captured after removing blurs, and grey-scale transform. To choose the candidates for the calibrating spot, we use a segmentation-based recombination and selection (SBRS) strategy, in which there appear no statistical uncertainty. Firstly, fluorescent intensity distribution of each sharp image is produced (Fig.3). Then, candidates emerge according to the following selection regulation. If $g_{i,j}$ is the grey scale of pixel(i,j), then the sum of grey scales of the adjacent pixels, $G_{i,j}$, is

$$G_{i,j} = \sum_{i,j} \begin{pmatrix} g_{i-1,j-1} & g_{i-1,j} & g_{i-1,j+1} \\ g_{i,j_1} & g_{i,j} & g_{i,j+1} \\ g_{i+1,j-1} & g_{i+1,j} & g_{i+1,j+1} \end{pmatrix}, \quad (6)$$

where i and j are the coordinates of pixels in individual sharp images. When the value of $G_{i,j}$ is maximum, $g_{i,j}$ is selected to be a candidate. Only one candidate for each image can enter the decisive stage. The final winner is defined as the referential location of the beam exit from the candidates set based on maximal probability.

Since the sample stage is used to move the reticule a fixed distance within the visual field of microscope and measure the corresponding number of pixels traversed, the calibration factors between μm and pixels under different objectives can be determined. Data of the calibration factors and origins are stored in a computer and used for all movement and measurement calculations. Based on the above origin, coordinates of the interesting point in each imaged cell can be set up. Then, a relationship is established between the pixel position of an object in the microscope camera and the real number of the x–y steps required to move the object to the microbeam exit. During cell irradiation, the XY sample stage locates cells one by one to the calibrating point along a preset route. A preset number of particles delivered to each cell are exactly controlled by a particle detector coupled with an electric beam-shutter. The manipulations above are all controlled by our developed program.

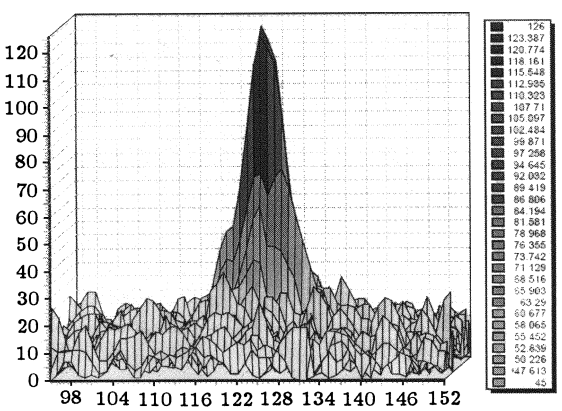


Fig.3. Side view of landscape of grey scales of individual pixels, showing the beam particle distribution.

3. Results

The normal energy of the CAS-LIBB microbeam is 3.0 MeV for protons, with the FWHM <40 keV after the 3.5-μm vacuum Mylar or the FWHM <64.5 keV after the multi-layer system. The average counting rate is 1000–2000 cps. Figure 4 demonstrates the results of Monte Carlo transport simulations of a 3-MeV proton beam. The diameter of the beam profile after monoenergetic protons passing through the collimator and traversing the multiplayer-film system perpendicularly is about 3.58 μm. Without the outmost vacuum Mylar ($C_{10}H_8O_4$), the diameter of the beam profile is about 3.03 μm.

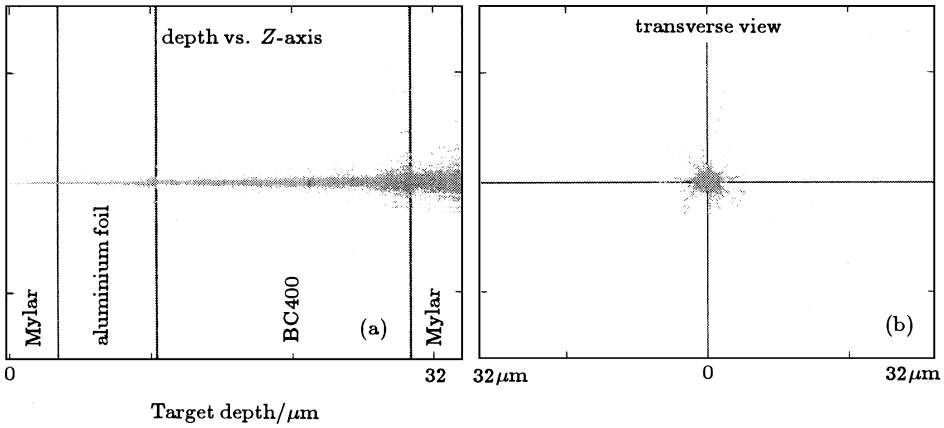


Fig.4. Beam profiles obtained by Monte Carlo transport simulation of 2000 3-MeV monoenergetic protons passing through the collimator and traversing the multiplayer-film system perpendicularly. (a) Beam profile along the Z-axis. (b) Transverse view.

The accuracy in measurements of the particle detection system and the cell targeting system is demonstrated using a CR39 detector (flaky form, 10mm×10mm×1mm). With the aid of the particle detection system, 100 protons are delivered to the CR39 surface to form a pit cluster (Fig.5). Analysis of 500 clusters shows that the average microbeam size is less than 5 μm in diameter for 81.78% of hits, less than 10 μm for 93.85% of hits or less than 15 μm for 98.75% of hits. Regarding the air gap between the mounting Mylar and CR39, Fig.5 shows a close agreement between the measured and predicted transmission profiles.

A series of fluorescent images of weak spots excited by traversing particles bombarding the scintillator is measured by the imaging subsystem. Figure 6

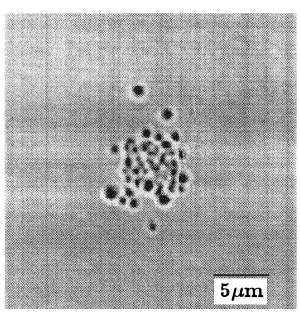


Fig.5. Confocal microscopy image of a 100-proton pit cluster etched on CR39.



Fig.6. A sharp image from a beam profile captured after grey-scale transform and invert contrast.

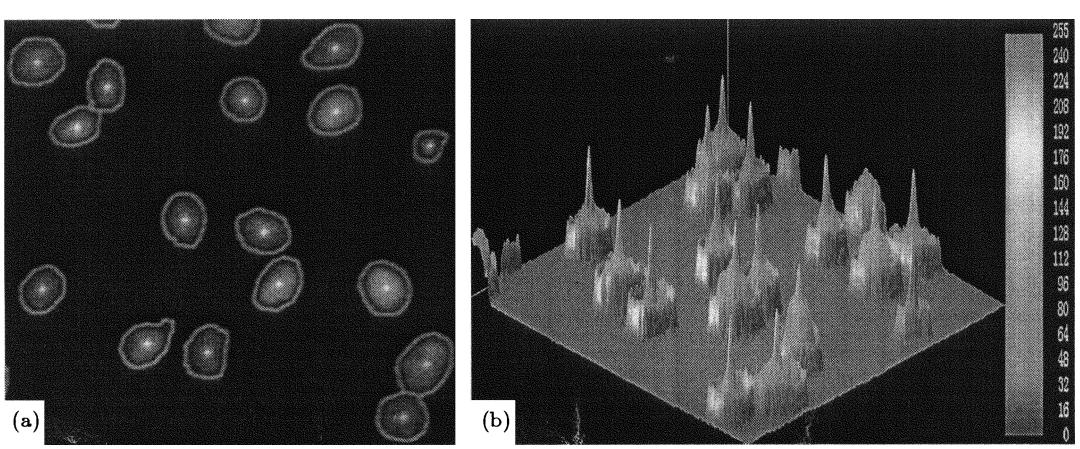


Fig.7. (a) Fluorescent image of monolayer-attached human epithelial cells stained with Hoechst 33342 dye, viewed by the image analysis system under a 40× objective lens. The nucleus of each cell is outlined. (b) The corresponding intensity 3D-peaks with an elevation angle 18° and a rotation angle 45°.

demonstrates a sharp image from a beam profile captured after grey-scale transform and invert contrast (Fig.6). The diameter of a typical beam profile after removing blurs is about 6.4μm. From images shown in Fig.7(a), individual monolayer-attached human epithelial cells and their nucleus are all recognized and marked by the image analysis system. Figure 7(b) shows the corresponding intensity 3D-peaks where the particles were delivered.

4. Discussion and conclusions

The overall cell targeting accuracy of the CAS-LIBB microbeam can reach $\sim 3\mu$m. For the two kinds of cells that are currently being researched in the laboratory, i.e. $A_{\rm L}$ cells (the average cross-sectional area of the nucleus of an attached living $A_{\rm L}$ cell was determined to be $108\mu{\rm m}^2$)[19] and AGO cells (fusiform, averagely 40μm wide and 100 μm long), the microbeam area confirms a sufficient spatial resolution. For an SPM, it is crucial to provide high speed and accurate radiation targeting for either cell or sub-cellular irradiation. The most important factor determining these performances is the ability of the mechanical assembly to position individual cells to the correct place accurately. To improve the target accuracy, several factors should be taken into consideration, including reducing the focal diameter of the beam, improving the cell finding efficiency, avoiding error propagation of cell positioning, elaborating the calibration procedure, and so on. Here, we discuss an important but less-regarded aspect—calibration procedure. On the other hand, this on-line approach can offer more microbeam characteristics of real-time beam profile than existing ones, such as beam halo, beam asymmetry and so on. Therefore, it makes possible optimizing the microbeam quality by further adjusting pertinent hardware setups.

References

[1] Mothersill C and Seymour C B 2004 *Nat. Rev. Cancer* **4** 158

[2] Legge G J F 1997 *Nucl. Instrum. Methods* B **130** 9

[3] Folkard M, Prise K M, Vojnovic B, Gilchrist S, Schettino G, Belyakov O V, Ozols A and Michael B D 2001 *Nucl. Instrum. Methods* B **181** 426

[4] Folkard M, Vojnovic B, Prise K M and Michael B D 2002 *Instrum. Methods* B **188** 49

[5] Brenner D J and Hall E J 2002 *Radiat. Prot. Dosim.* **99** 283

[6] Folkard M, Vojnovic B, Gilchrist S, Prise K M and Michael B 2003 *Nucl. Instrum. Methods* B **210** 302

[7] Hu Z W, Wu L J and Yu Z L 2005 *Plasma Sci. Technol.* **7** 2789

[8] Hu Z W, Yu Z L, Wu L J, Hu S H and Xu A 2003 *Nucl. Instrum. Methods* A **507** 617

[9] Wang X F, Wang X H, Chen L Y and Hu Z W 2004 *Chin. Sci. Bull.* **49** 1806

[10] Wang X F, Chen L Y, Hu Z W, Wang X H, Zhang J, Li J, Chen B, Hu S H, Shi Z T, Wu Y, Xu M L, Wu L J, Wang S H and Yu Z L 2004 *Chin. Phys. Lett.* **21** 821

[11] Wang X F, Hu Z W, Wang X H, Chen L Y, Zhang J, Li J, Wu Y, Chen B, Wu L J and Yu Z L 2004 *Chin. Phys. Lett.* **21** 1922

[12] Wang X H, Wang X F, Hu Z W, Cheng L Y, Zhang J, Zhan F R, Li J, Chen B, Xu M L, Wu L J, Wang S H and Yu Z L 2005 *Chin. Phys.* **14** 1277

[13] Folkard M, Vojnovic B, Prise K M, Bowey A G, Locke R J, Schettino G and Michael B D 1997 *Int. J. Radiat. Biol.* **72** 375

[14] Randers-Pehrson G, Geard C R, Johnson G, Elliston C D and Brenner D J 2001 *Radiat. Res.* **156** 210

[15] Badhwar G D, Deney C L, Dennis B R and Kaplon M F 1967 *Nucl. Instrum. Methods* **57** 116

[16] Birks J B and Brooks F D 1956 *Proc. Phys. Soc.* B **69** 721

[17] Birks J B 1964 The Theory and Practice of Scintillation Counting (New York: Pergamon) p62

[18] Craun R L and Smith D L 1970 *Nucl. Instrum. Methods* **80** 239

[19] Hei T K, Wu L J, Liu S X, Vannais D, Waldren C A and Randers-Pehrson G *Proc. Natl. Acad. Sci. USA* **94** 3765